WIND DRIVEN CURRENTS SOUTH OF OAHU

A THESIS SUBMITTED TO THE GRADUATE DIVISION OF THE UNIVERSITY OF HAWAI‘I AT MĀNOA IN PARTIAL FULFILLMENT OF THE REQUIREMENTS FOR THE DEGREE OF

MASTER OF SCIENCE

IN

OCEANOGRAPHY

AUGUST 2014

By
Alma Carolina Castillo Trujillo

Thesis Committee:

Pierre Flament, Chairperson
Brian Powell
Glenn Carter

We certify that we have read this thesis and that, in our opinion, it is satisfactory in scope and quality as a thesis for the degree of Master of Science in Oceanography.

THESIS COMMITTEE

_____

Chairperson

_____

_____

Abstract

Wind Driven Currents South of Oahu

Two years of HFDR currents south of Oahu were analyzed to understand the main modes of circulation. A relatively slow ($\approx$ 20 cm/s) westward flow was observed with eastward reversals in winter and spring. To understand these reversals, their dependence on local wind forcing was investigated using buoy measurements and a 1.5-km resolution operational atmospheric model. Southerly winds were typically found when the reversals occurred. The dominant EOF mode accounts for 58% of the variance, and is significantly correlated with the meridional wind. To further assess the effect of the winds, the vorticity balance was estimated. The advective non-linear term is mostly balanced by vertical stretching of the water column and a residual term derived from the sum of those two terms. This residual term, is significantly correlated with the wind stress curl term derived from an atmospheric model, indicating that it is the main external forcing in the vorticity generation. An operational ROMS nested model for the Hawaiian Archipelago is used to understand the vertical behavior of the wind driven currents. Vertical modes computed from model currents are well correlated with both the wind and wind stress curl during trade wind conditions and suggest a rapid decay of wind effects below the Mixed Layer Depth.

Acknowledgements

First of all I will like to thank my advisor Dr. Pierre Flament, along my advisory committee Dr. Brian Powell, Dr. Glenn Carter and Dr. João Souza for their help, feedback and intellectual support.

Thanks to all the radlab members (Benedicte Dousset, Maël Flament, Charina Repollo and Dave Harris), for their help and friendship since the beginning of the graduate program.

Special thanks to Ken Constantine, Paul Lethaby, Xavier Flores, Mayra González, Jean-Phillipe Derout, Matt Archer, Jhobert and Hayden Repollo, Colette Kerry, YuWei Chan, Ian Quino, Marco Larrañaga, Juan Gomez and Jake Cass for their support on the radar installations. Thanks to the administrative staff at UH; Lance Samura, Kristin Uyemura and Catalpa Kong.

Thanks to all the graduate students at UH, specially Svetlana Natarov, Lindsey Benjamin, Oyvind Lundesgard and Seth Travis for their feedback on this work and the stimulating scientific discussions in and outside classes.

Special thanks to all the friends I have met in Hawaii and now have become my family; Fabio, Renata, João, Clara, Tom, Francois, Adam, Sara, Scott, Fernando and Pavitza.

Thanks to my family in Mexico, mom, dad, sister and friends. "Papá y Mamá, ustedes son la razón por la que estoy aqui. Ilse, además de mi hermana, mi mejor amiga. Osvaldo y Oscar mis hermanos postizos, y todos los demás amigos que me han apoyado a traves de estos años especialmente Alejandra, Nallely, Sandra, Marco y Jey."

Finally, thanks to Saulo for his patience and encouragement. With you I am a better person.

...

Contents

List of Figures

A mis padres...

Chapter 1

Wind Driven Currents

1.1 Introduction

The Hawaiian islands are located in the midst the North Pacific Oceanic gyre. The westward North Equatorial Current (NEC) encounters the islands and bifurcates into the North Hawaiian Ridge Current (NRC) to the north and the Hawaiian Lee Current (HLC) to the south of the archipelago. South of the HLC; the Hawaiian Lee Counter Current (HLCC) flows eastward it bifurcates and reverses to contribute to the HLC and NEC [Lumpkin, 1998; Qiu et al., 1997; Lumpkin and Flament, 2013].

The strong atmospheric subtropical high pressure system generates a consistent trade wind pattern in the Hawaiian chain that creates dipoles of positive and negative wind stress curl in the western and eastern lee of the islands due to a blocking

effect by the mountains. Moreover, this mechanism drives divergent and convergent Ekman transport which is compensated by vertical water motions which in turn move the thermocline up and down resulting in cyclonic and anticyclonic eddies [Lumpkin, 1998]. Chavanne et al. [2002] developed the Sverdrup solution from satellite winds concluding that wind stress curl acts as the forcing mechanism that creates the HLCC and balances the meridional flow in the Hawaiian Islands. This wind stress curl mechanism has been observed in many islands and coasts around the world [Chelton et al., 2004; Barton et al., 2000; Pullen et al., 2008].

Observational studies south of the Hawaiian archipelago have indeed shown strong cyclonic and anticyclonic areas in the lee of the islands [Lumpkin and Flament, 2001; Patzert, 1969; Lumpkin, 1998]. A recent Model by Calil et al. [2008] has shown stronger cyclonic eddies were generated when stronger and persistent trade wind forcing was present. They also concluded the absence of eddy formation in the lee of the Big Island during windless periods. Chavanne et al. [2010] also found anticyclonic areas north west of the islands using High Frequency Doppler Radios (HFDR).

However, the lack of resolution in previous studies makes it difficult to understand the time and spatial scales of the wind variations and thus the response of the upper ocean. Two HFDR have been measuring ocean surface currents off the south shore of Oahu since 2009, at a high spatial and temporal resolution enabling the detection of sub-mesoscale and mesoscale level processes.

1.2 Methodology

1.2.1 High Frequency Doppler Radars

Two years of HFDR from August 2010 to September 2012 are analyzed. Each HFDR works as a Frequency Modulated Continuous Wave operating at 16 MHz with 100 kHz chirp width yielding a spatial resolution of $\approx 1.5km$, [Gurgel et al., 1999]. Measurements are averaged every 11.6 minutes yielding a 15 min temporal resolution due to HFDR processing.

Each site has a linear array of antennas, the westerly site in Kalaeloa ($21°17.76'N$ $158°5.17'W$) is oriented 235° from the north while the easterly side in KokoHead ($21°25.62'N, 157°42.26'W$) is oriented 310° (Figure 1.1), both are operating with 4 transmit antennas in a squared array. Transmit antennas form a beam towards the ocean and a null towards land. By the Doppler shift of radio waves Bragg-scattered by surface gravity waves of half the electromagnetic wavelength (16 MHz, lambda=9.35 m), each HFDR measured the radial component of the current in the direction of the instrument. The two sites are used to compute vector currents by least squares fitting the radial components on-to a 2-km cartesian grid. The beam-formed array results in an azimuthal resolution of $\approx 7°$ with a working range of $\approx 100km$ from the coast.

A Geometric Dilution of Precision (GDOP) results [Chapman et al., 1997] from HFDR grid points falling near the baseline and far from the HFDR sites yielding

poorly constrained azimuthal components when vector currents are calculated see Appendix B. To eliminate spurious data, grid points with a GDOP bigger than 1.3 were eliminated. Ionospheric variations in the atmosphere and system failures also resulted in missing data. Values that have less than 50 % of data coverage were also removed, small data gaps less than 2 days were interpolated by least square fitting sinusoids at M2, K1 and inertial frequency following Chavanne et al. [2007].

Figure 1.2 shows spatially averaged rotary spectra for the whole data set. Semidiurnal tides dominate the super-inertial bands with diurnal tides significantly weaker. Clockwise energy is larger than counterclockwise in the inertial band with the strongest near inertial peak shifted from the main inertial period, 33 hours for this area, while the lower frequencies regions seem to have stronger clockwise energy. Higher frequencies show no rotary asymmetry. Tidal oscillations were removed to reduce spectral leakage into lower frequencies with the t-tide package [Pawlowicz et al., 2002]. A 3-day Butterworth low pass filter was then applied to the detided data to reduce inertial oscillations, linear interpolation was made to remaining gaps.

1.2.2 Wind Measurements

Three years of wind measurements every 6 minutes were extracted from National Data Buoy Center (NDBC) OOUH1 wind station located at 9 m above sea level $(21°20.5'N, 157°53.4'W)$. A 3 day- Butterworth low pass filter was used to remove

diurnal and inertial variability from hourly averaged data. A Weather Research Forecast (WRF) model developed at University of Hawaii at Manoa, customized for the Hawaiian islands, was used to calculate wind stress curl at a 4 hour and 2.2 km temporal and spatial resolution respectively. These values were then interpolated on the same spatial and temporal grid as the HFDR data. Wind stress from the WRF model was computed following Large and Pond [1981] as $\tau = \rho Cd|w|w$ where ρ has a constant value of 1025 kg/m^3, Cd is a variable drag coefficient and w is the wind referenced to 10 m. To validate the WRF model, a complex lag correlation was calculated between the NDBC buoy data and the closest wind model data point, resulting in a significant maximum correlation of 0.75 at 0 lag. All correlations in this paper are made at a 95% significance level as follows [Kundu, 1976]:

$$\rho(\mathbf{x}_1, \mathbf{x}_2, \tau) = \frac{\langle w_1^*(t) w_2(t+\tau) \rangle}{[\sqrt{\langle w_1^*(t) w_1(t) \rangle} \sqrt{\langle w_2^*(t) w_2(t) \rangle}]} \tag{1.1}$$

Where $w = u + iv$, subscripts 1 and 2 denote two different time series and over-bars denote the time or ensamble average. The correlation ρ, which is independent of the choice of coordinate systems, is a complex quantity whose magnitude gives the overall measure of correlation and phase gives the average clockwise angle of the first vector with respect to the second.

1.3 Results

1.3.1 Mean Flow and Vorticity

The mean circulation over the two year record consists of a westward flow through the whole HFDR coverage area, with stronger speeds of up to 30 cm/s found in deeper waters (Figure 1.3), consistent with the HLC seen by drifters ([Lumpkin and Flament, 2013]).

Time series of the HFDR currents averaged over the whole domain are shown in Figure 1.4. They have a mean magnitude of 25 cm $\pm$ 11 cm σ. During summer (months 05-09), the alongshore component is westward while the cross shore component is variable and weaker except for late summer on 2012. During winter and spring months (01-04 months) south and east-ward currents are observed while on fall current resembles summer behavior.

Different spatial patterns are observed depending on the time of the year (Figure 1.5). For February 2011 averaged currents, a southward flow with speeds of up to 20 cm/s and weaker values towards the Kaiwi channel were observed. In May 2011, a north-east flow is observed in most of the coverage area with currents toward the Kaiwi channel. In August 2011 and October 2011 a westward averaged flow with speeds increasing away from the coast is seen. The northern half of a cyclonic eddy is observed deeper than the 1000 m isobath in August 2011. Cyclonic eddies

similar in size are seen throughout the entire HFDR time series moving north-east towards the Penguin Bank area.

Monthly averaged relative vorticity normalized by Coriolis frequency is also shown in Figure 1.5. High positive (cylconic) values are found close to the coast during February 2011. This area of cyclonic circulation extends all the way to the east in May 2011. August 2011 shows strong negative values close to the coast and positive values farther than the 1000 m iso-bath, where a cyclonic eddie is seen moving towards Penguin Bank. October 2011 has positive vorticity values of ≈ 0.4 in Kaiwi channel while the rest of the area shows negative values of ≈ -1.2. Absolute vorticity seems conserved as currents follow vorticity contours except for October were vorticity was weaker and the westward flow.

1.3.2 Wind driven currents

Two years of low-pass filtered wind time series from the NDBC stations are shown in figure 1.4b, north-easterly trade winds dominate with small sporadic south-westerly reversal events (know locally as Kona winds). Current reversals are observed mostly from fall to spring where Kona winds are present (Figure 1.4a). Figure 1.4c shows the low-passed winds from the WRF model at the grid point where values where most significantly correlated to the HFDR currents, figure(1.6a). WRF wind magnitude values varied between 10 and 15 ms^{-1} compared to NDBC wind station where values ranged between 5 and 10 ms^{-1}, this underestimation of

the NDBC winds is due to the effect coastal processes in the station. Correlation between NDBC wind station and model yielded 0.79 at 0 time lag. Although the WRF model does not fully represent all southerly wind periods, for the purpose of this thesis the WRF model seems a reliable source of measurement since its spatial coverage encompasses the whole HFDR coverage and thus allows a detection of wind-wake effects due to the islands.

To understand the coherence between low passed wind and currents, a normalized complex lag correlation was computed (eq 1.1). Figure 1.6a shows only the 95% significant correlations between the low-passed WRF wind and low passed HFDR vector currents at each grid point. Correlations greater than 0.30 are seen mainly on the Kaiwi channel and in the center of the domain, suggesting areas where wind is important in dominating the currents, although smaller values of correlation close to the coast and away from the HFDR could be associated to radar noise due to GDOP, wind does seem to be an important factor affecting the currents. To further prove that, the clockwise angle between wind and currents is shown in Figure 1.6b, results were consistent with Ekman Theory were given constant vertical eddy viscosity and infinite depth, it predicts surface currents 45° clockwise from the wind. Current angles ranged between 45° and 100° clockwise from the wind where correlation values were significant. Although most of the values were found around 60°, smaller values of $\approx 30°$ were found in the Kaiwi Channel area and higher values were found on Penguin Bank $\approx 90°$ showing that topography may have an effect on current behavior due to the wind.

1.3.3 Wind stress curl

It is clear that wind has a significant effect on the currents, but can model detect the dipoles of positive and negative Wind Stress Curl in the lee of the islands? Figure 1.7 shows the Wind Stress Curl for different months of 2011. There is a clear seasonal pattern throughout the year, in February 2011 (Figure 1.7a) the averaged wind stress curl is small compared to all other months. Since south-westerly events are present (Figure 1.4), Oahu no longer blocks the wind, and thus the wind stress curl lessens. May and August (1.7b,c) show the most prominent dipoles of positive and negative wind stress curl with values of $3 \times 10^{-6} Nm^{-3}$. When trade winds are persistent, Penguin Bank area shows positive values from the shadow of Maui. In the rest of the HFDR domain, negative wind stress curl is observed from the wind-wake of Oahu. When winds come from the south, the wind curl is small since the shadow effect of Oahu disappears, while during trade winds, Oahu generates a shadow that increases curl on either side of the island. Furthermore, the topography close to the islands generates dipoles of positive and negative wind stress curl ($1 \times 10^{-6} Nm^{-3}$). (Figure 1.4).

1.4 Discussion

Two years of high-resolution (1.5 km) HFDR surface current observations revealed the main current variability south of Oahu is due to the wind. The two year

mean shows a westward flow with stronger speeds in deeper waters (Figure 1.3). Previous studies have shown the westward HLC measured with drifter buoys south of Hawaiian Islands orginiated from the NEC, [Firing et al., 1999; Lumpkin and Flament, 2013], since the net effect of the presence of the islands is to induce accelerated jets on the southern and northern end of the islands generating the HLC and HLCC.

There has not been a regional study of the area at the same spatial and temporal resolution other than Cass [2010] who used radial currents from one radar site and found stronger speeds during summer months. On a larger scale, [Lumpkin and Flament, 2013] found higher velocity values of the HLCC for summer and winter months and weaker in spring. Since the formation of the HLC is dependent on the HLCC [Qiu and Durland, 2002; Kobashi and Kawamura, 2002] and our results show a westward stronger flow in December and August while weaker and sometimes eastward flows from February to May, there may be a direct correlation in surface dynamics south of Oahu with the HLCC. Further more [Lumpkin and Flament, 2013] showed a northwest flow of the HLCC in January and April. Figure 1.4 also showed northward currents for May which can be associated to the HLCC variability seen by literature.

Surface currents in figure 1.4 showed a seasonal pattern with stronger westward flows in summer 2011 and winter 2011-2012 while eastward flows at the end of winter and spring months. Since these reversals were found when southwest winds events appeared that is winter and spring primarly, they can be a consequence

of the weaker HLC and the south west winds. Figure 7 showed the strong correlation between winds and currents with the angle between them consistent with Ekman Theory, these angles showed values between 45° and 100° clockwise from the wind to the currents where correlations were significant, the bigger angles can be related to a shallow mixed layer in the area since turbulent mixing is trapped on a smaller layer thus increasing the angle between wind and currents to more than the expected 45 ° due to Ekman theory [Schudlich and Price, 1998].

It is clear that the main current patterns south of Oahu are driven by the wind, evidence of that is shown by the first two modes of the Empirical Orthogonal Functions (EOF) (Figure 1.8). EOF 1 accounted for 58% of the variance and it seems related to the meridional wind, since its reconstructed **u** and **v** mean components showed a north east flow and its associated Temporal Function (TEOF) (Figure 1.9) showed strong positive values in winter while negative and weaker values in summer. EOF 2 accounted for 12% of the variance and its mean reconstructed currents were associated to a cyclonic/anticylonic circulation with stronger values in the areas of strong Wind Stress Cur. To further prove that, the associated Temporal Function of EOF 1 was significantly correlated to the meridional wind (figure 1.9) while the temporal EOF 2 function was significantly correlated to the wind stress curl derived from the WRF model (Figure 1.7). It is important to mention a third significant EOF accounted for 5% of the total variance and was not not correlated to the wind either spatially of temporally, but its spatial function was larger in the 50 m Penguin Bank (Figure 1.9) revealing the impact of

topography in the surface currents at smaller scales.

Several cyclones were seen on the HFDR currents south of Penguin Bank flowing westward towards the Kaiwi channel, where positive wind stress curl was seen (Figure 1.7). It is known that strong mesoscale eddies are generated in the region due to the positive wind stress curl and/or fast westward flows through channels between islands [Chavanne et al., 2002; Jia et al., 2011]. When a cyclonic circulation was observed, trade wind events are found as seen by the significant correlation of the spatial EOF2 with the wind stress curl (Figure 1.7). Models have shown stronger eddies at a 0.1° resolution than 0.25° resolution [Yu et al., 2003], even though it is not quite well understood the impact of smaller wind stress curl variations, satellite observations by Chelton et al. [2004] showed that stochastic forcing by the energetic small-scale variability in the wind stress curl field may play an important role in the generation of eddies in the ocean

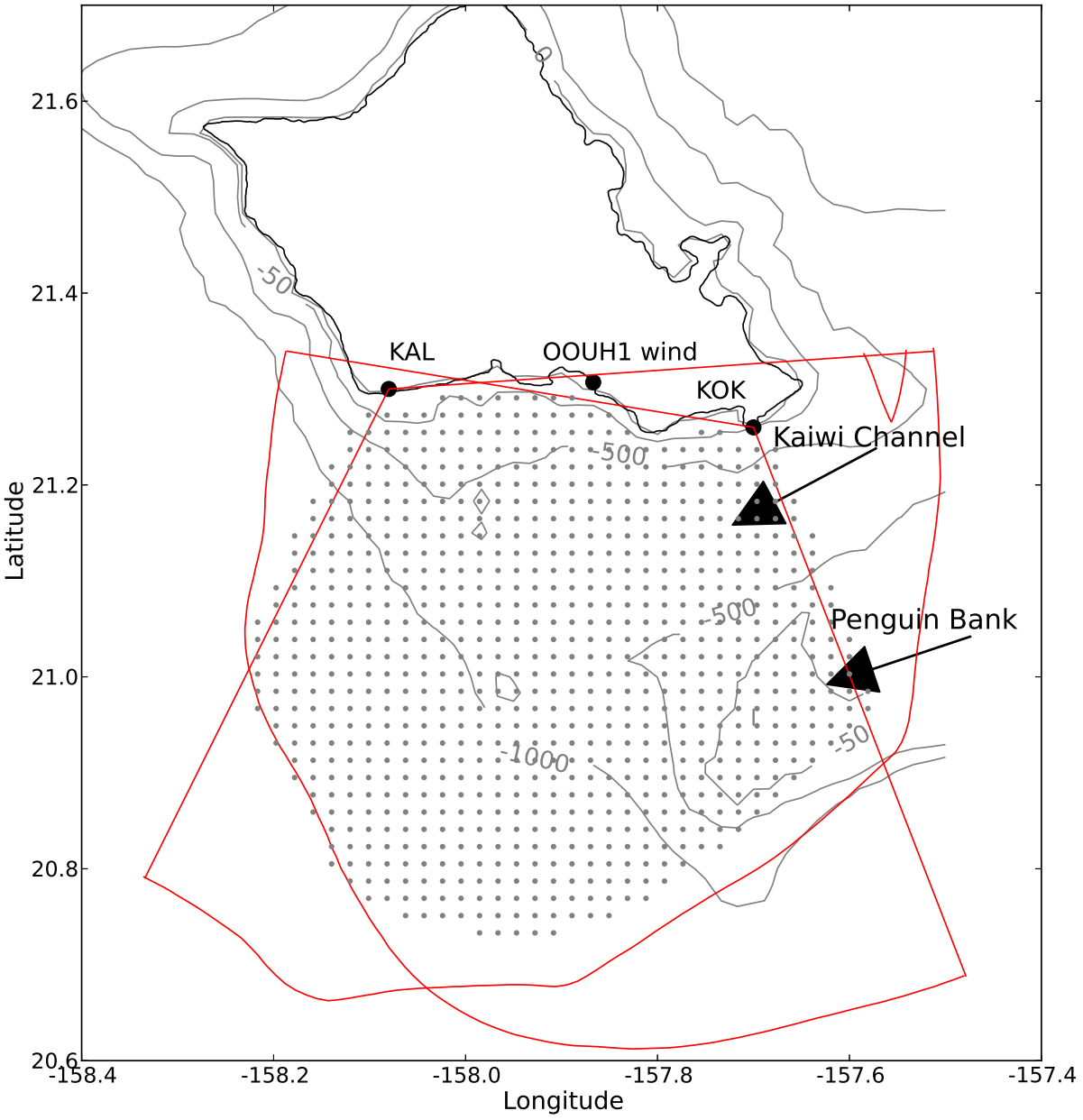

FIGURE 1.1: South of Oahu study area. HFDR are denoted with black dots. (KAL, Kalaeloa; KOK, Kokohead). The red lines indicate the 50% HFDR radial coverage for each site. Small gray dots indicate the grid points where U and V currents were computed. NDBC OOUH1 wind station is also shown. The 50, 100 and 1000 iso-bath contours are plotted in grey lines

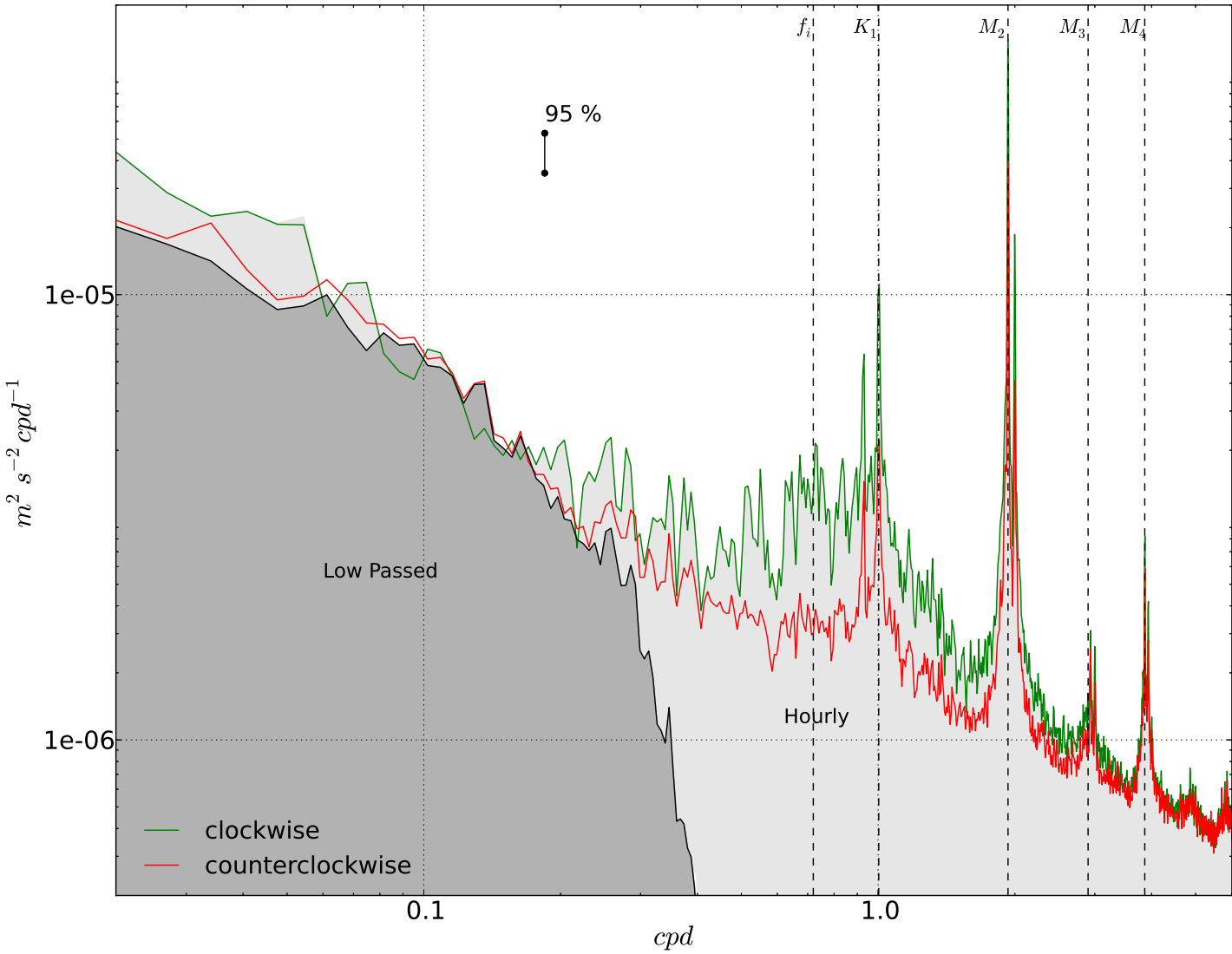

FIGURE 1.2: Rotary power spectrum averaged over the whole HFDR grid from hourly data. Tidal Constituents and inertial frequency f_i are indicated on the top x axis. Dark grey and light grey area show the three day low passed filter and raw data respectively. 95% significant error bars are also shown.

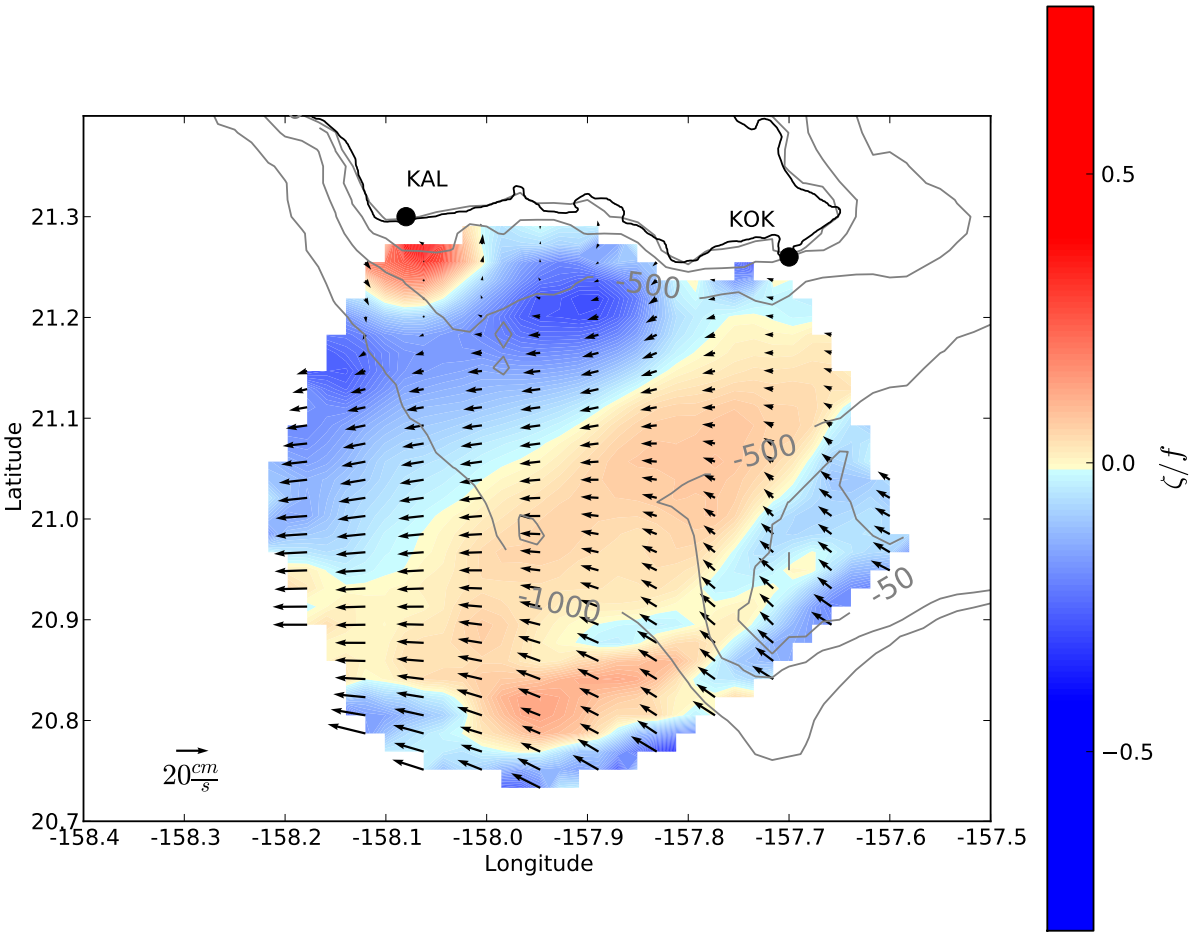

FIGURE 1.3: Two year monthly mean flow from September 2010 to August 2012. Thin grey lines indicate bathymetry in meters. Colorbar indicates normalized vorticity for the same period. Colorbar indicates normalized vorticity.

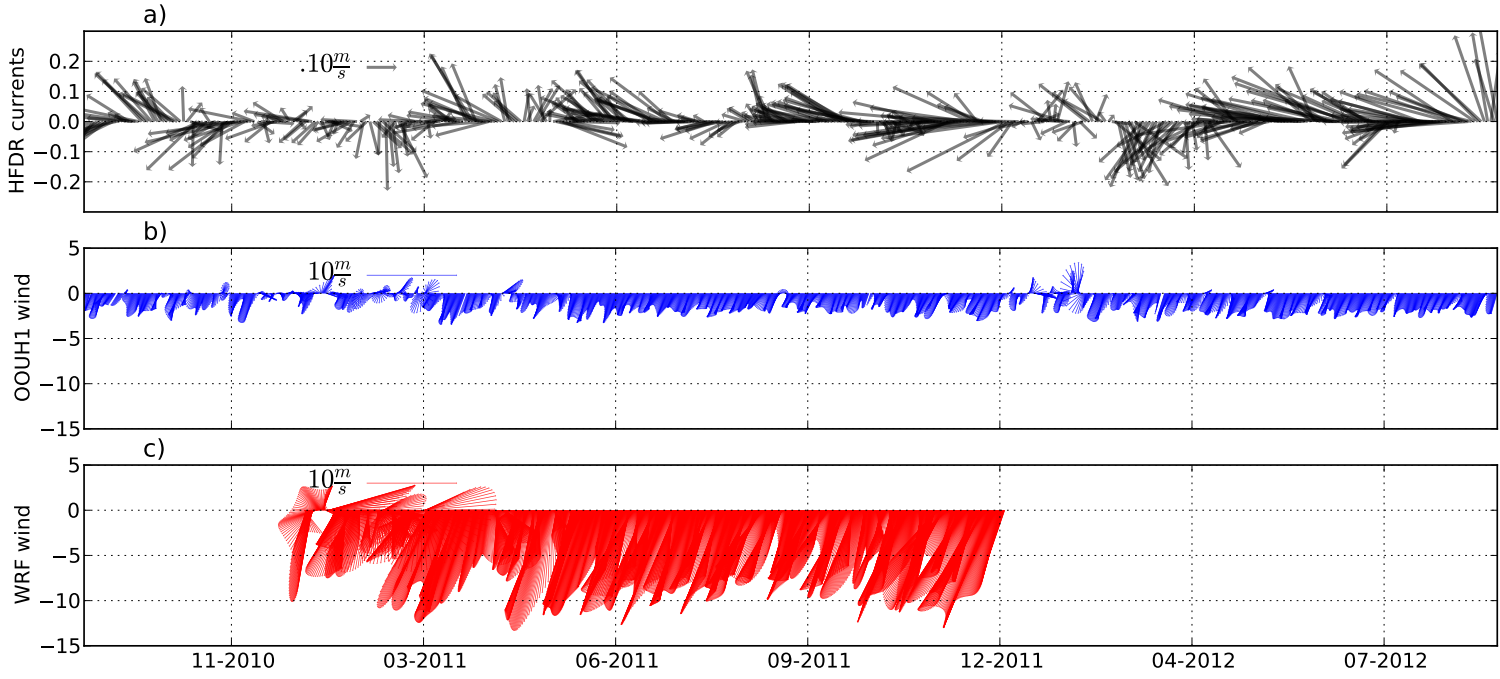

FIGURE 1.4: a)Time series of averaged HFDR low pass filtered currents over the whole domain in Figure 1. b)low passed wind station from NDBC OOUH1 (bottom row). c)WRF operational wind model where wind and currents were best correlated, See Figure 1.6.

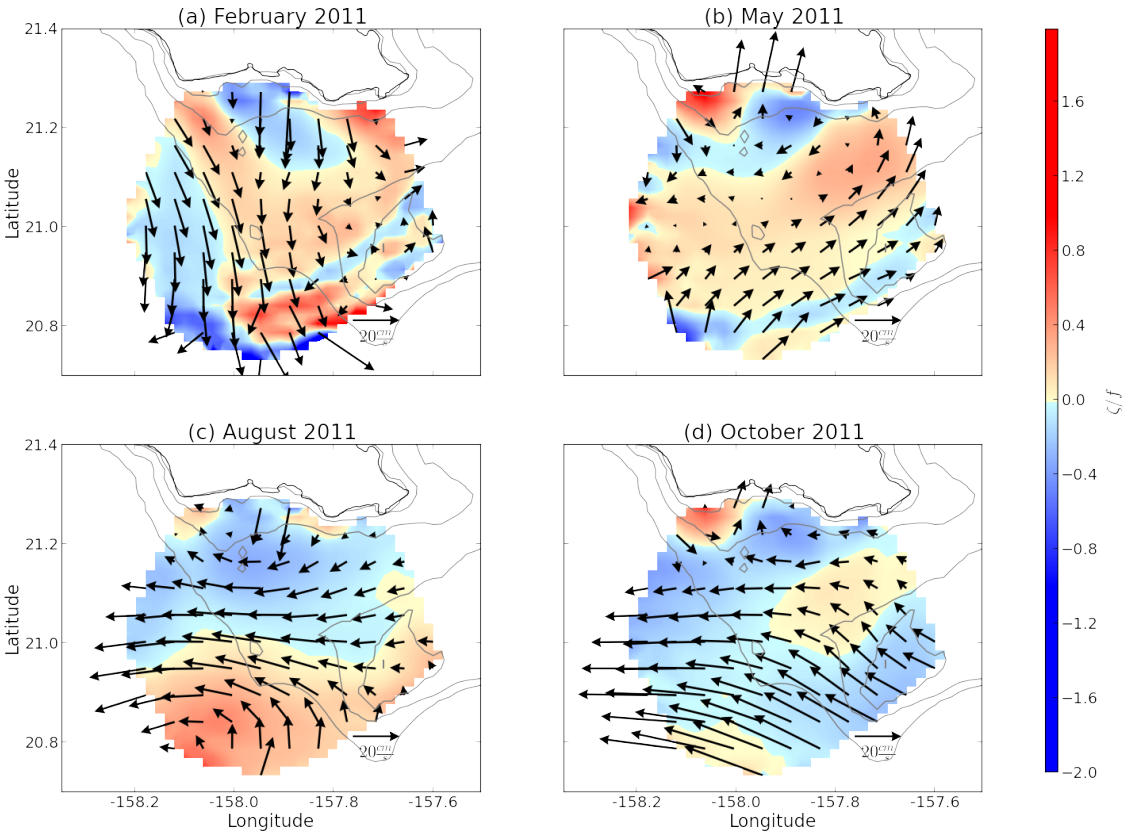

FIGURE 1.5: 2011 Mean monthly HFDR surface currents velocities for (a) February, (b)May, (c)August and (d)October. Colors indicate relative vorticity normalized by Coriolis parameter.

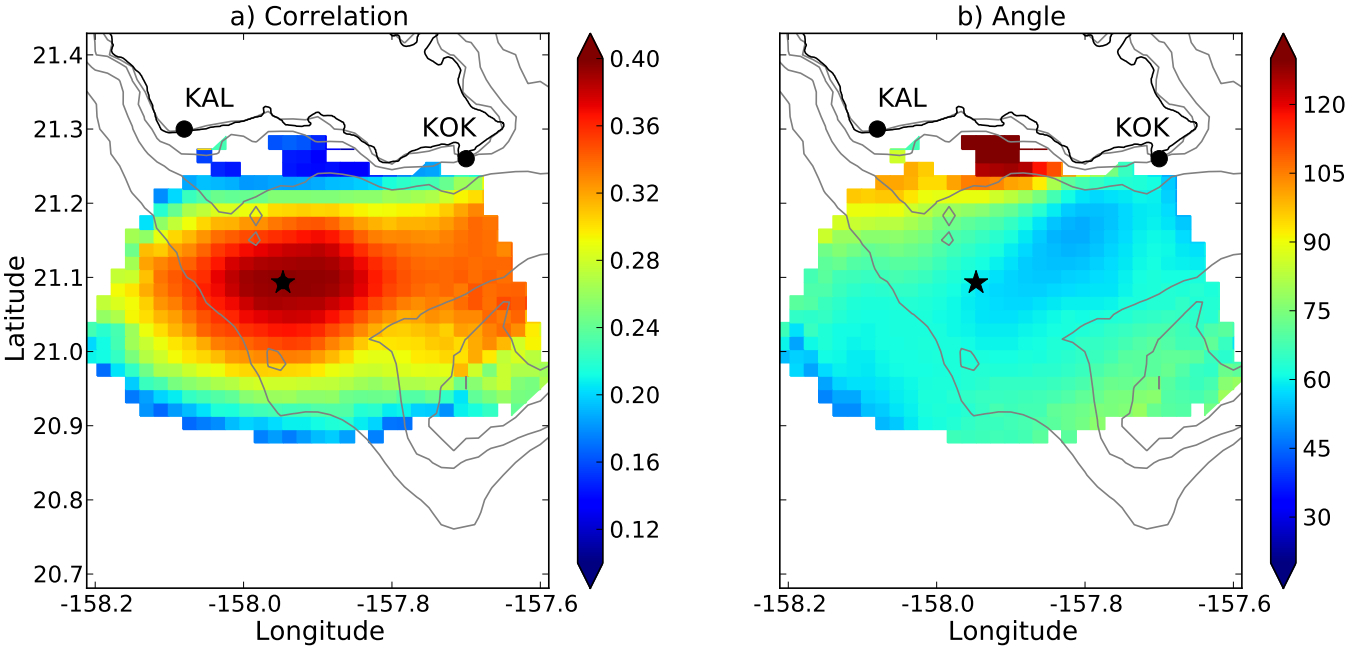

FIGURE 1.6: Cross correlation (Left) and clockwise phase angle (Right) between WRF wind model and HFDR low-pass surface currents. Black star indicates the grid point where highest correlation was found. Only 95% significant level values are shown.

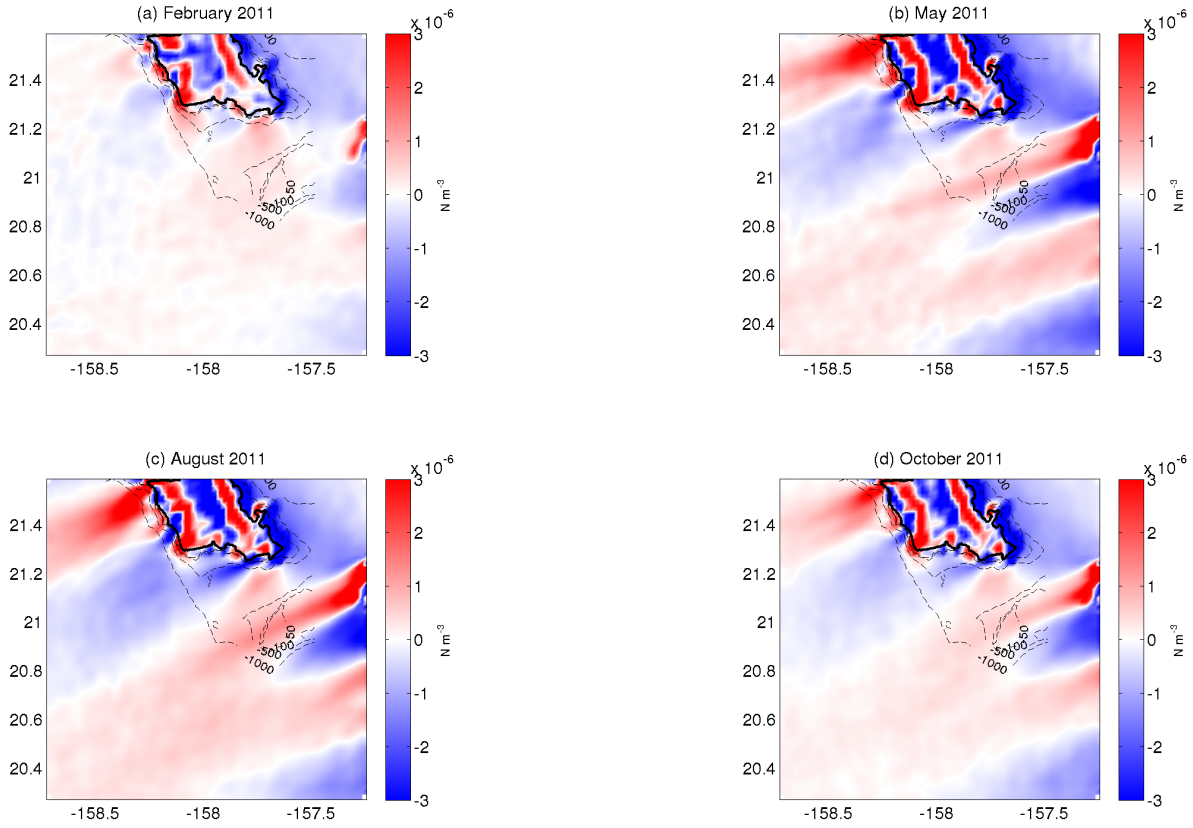

FIGURE 1.7: 2011 monthly wind stress curl derived from the WRF wind model for (a) February, (b) May, (c) August and (d) October.

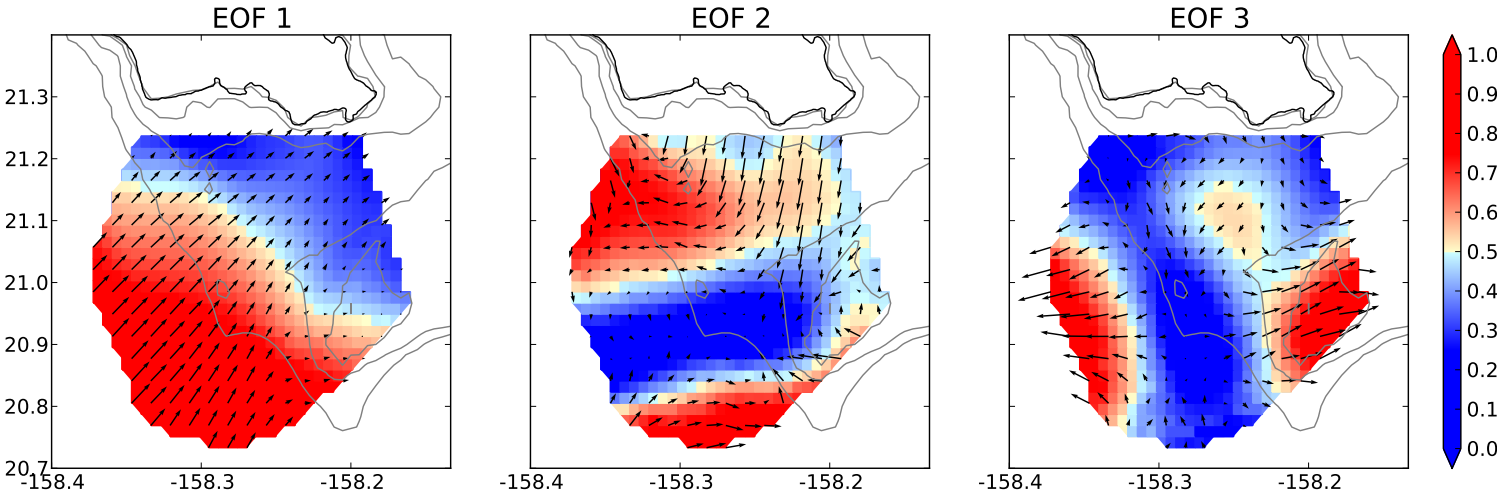

FIGURE 1.8: Significant spatial Empirical Orthogonal Functions (EOF) for the whole time series. (a)EOF 1,2 and 3 accounted for 58%, 12% and 7% of the variance respectively. Averaged reconstructed EOF surface currents are also indicated by black arrows on each figure.

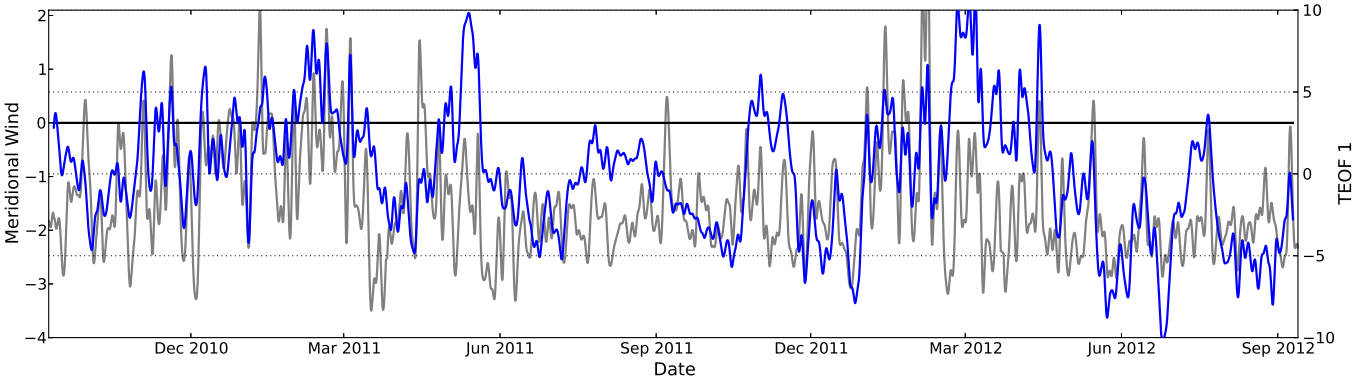

FIGURE 1.9: 3 day low passed meridional wind from OOUH1 wind station (gray line) and its first Temporal Empirical Orthogonal Function (blue line). Correlation between the two time series yields 0.4 at 95% significance level

Chapter 2

Vorticity Balance

2.1 Introduction

Taking advantage of the HFDR capabilities, we quantify the forcing mechanisms in the surface currents south of Oahu and compare different patterns of circulation when wind varies from north-east to south-west. To quantify the forcing mechanisms, a vorticity balance is calculated, in which the wind is obtained from the atmospheric WRF wind model interpolated on-to the HFDR temporal and spatial grid.

2.2 Methodology

By taking the curl of the momentum equation:

$$\frac{D\mathbf{u}}{Dt} + f \times \mathbf{u} = -\frac{1}{\rho}\frac{\partial P}{\partial \mathbf{x}} + \mathbf{F} \tag{2.1}$$

we arrive at the vorticity balance

$$\frac{D\zeta}{Dt} + (\zeta + f)\left(\frac{\partial u}{\partial x} + \frac{\partial v}{\partial y}\right) + v\beta = \nabla_z \times \mathbf{F} \tag{2.2}$$

First term of eq(2.2) is $\frac{\partial \zeta}{\partial t} + \mathbf{u} \cdot \nabla \zeta$, second term is vortex stretching, when integrated over depth, this stretching term relates to the difference between vertical velocities at the surface and at the bottom of the layer, and the third term is the variations of the coriolis parameter f with respect to latitude. The term on the right hand side is the external forcing and is calculated as a residual from the terms on the left hand side of eq (2.2) and by assuming F is Wind Stress Curl derived by the WRF wind model used in previous chapter. To reduce noise from derivations, vorticity equation terms were calculated by least square fitting the gradients of an area defined as the 3-km radius closest to each HFDR grid point. Thus, the resulting slope was then used as the final gradient on each point. Time gradients were computed every 24 hours.

2.3 Results

Figure 2.1 (first three columns) shows the vorticity equation terms derived by the HFDR, neglecting the variations of planetary vorticity in latitude since they

were an order of magnitude smaller than the remaining terms. When averaged over 2011, the vorticity equation is primary balanced between the stretching and external forcing term with a smaller role for the advective term. Positive (negative) values were found in the southeast (northwest) part of the domain for all the terms. The stronger values are found close to the Penguin Bank and Kaiwi channel. The advective term although half an order smaller than the other terms has a similar spatial behavior as the forcing term.

The previous section showed the difference in wind stress curl when wind changes in direction during 2011, that is trade winds in summer and south-west winds in winter and spring. To illustrate the vorticity spatial distribution for the two most common wind directions in the area, Figure 2.1, middle row shows vorticity terms for a typical month with southwest winds (February 2011) and bottom row with northeast winds (August 2011). For both months there is an even balance between the three terms. February shows positive and negative values spread all over the area, while August shows strong positive values in the south part of the area. The advective term in both months follows similar patterns as the forcing term computed as a residual from the balance, suggesting external forcing as the main process generating advection of the vorticity.

If we assume that wind is the main frictional process at the ocean surface and that at a given Ekman depth, H_E, the wind stress, τ, vanishes as $\tau = \tau_w[1 - \frac{z}{H_E}]$. The wind driven component in the momentum equation (2.1) is simply $F = \frac{1}{\rho_o}\frac{\partial \tau}{\partial z}$, taking the curl of F and assuming currents are depth-independent over H_E. The

residual term from the vorticity equation (2.2) (Figure 2.1 third column) can be compared to the following wind term: $\frac{1}{\rho_o H_E}\nabla_H \times \tau$. Where τ is wind stress calculated from the WRF wind model in previous section, H_E is assumed to be 10 m which is the averaged Ekman depth found in the area and ρ_o is the density of seawater assumed to be constant at $1025 kgm^{-3}$ (Figure 2.1 fourth column). Both terms should agree if wind is indeed the main forcing mechanism. While the wind forcing term shows positive values observed in Penguin Bank all the way to the 1000 m iso-bath, the residual term seems to be positive only in Penguin Bank and Kaiwi channel. For both February 2011 and August 2011 averaged terms, wind stress curl follows similar spatial patterns as the residual term but in smaller magnitude. There is a strong residual term south of KOK and KAL that is also apparent in the wind stress curl from the model. It is remarkable the difference in patterns for a month where trade winds are present like August 2011, where positive wind stress curl is only on the Penguin Bank Area to a month like February where south western winds are sporadic throughout the month and wind stress curl appears as strong as in August but dispersed through the whole grid. This suggests the wind as the main forcing affecting the vorticity in different ways depending on the direction and magnitude of the wind. The advective term in August is positive in the southwest of the area where the cyclonic eddie is seen.

A cross correlation between daily averaged forcing term derived as the residual from the vorticity balance (solid black line) and averaged wind term derived by the WRF model (pink line) is shown in figure 2.2. Even though results for February,

May, August and October 2011 were significant, only in August both terms seem to follow similar patterns in magnitude and time, in contrast, October 2011 residual term appears significantly smaller than wind-forcing. Even though, the spatial similarity between the terms is an indication that the WRF atmospheric model is indeed representing correctly the wind as the main external forcing in the vorticity balance.

2.4 Discussion

HFDR observations allowed the detection of small scale vorticity generation processes. External forcing is certainly derived by the wind since there is a strong similarity between the forcing term derived as a residual from HFDR and wind forcing term derived from the WRF model. For 2011 averaged terms, the positive values derived from the wind in the area were significantly correlated to the residual term, this forcing is due to the trade wind pattern generating positive wind stress curl from the cluster of islands east of Oahu (Molokai, Lanai, Maui), [Chavanne et al., 2002]. The stretching term also showed similar spatial pattern as the wind term, since it is clearly related to the cyclonic circulation from the trade winds seen throughout the HFDR data set (Figure 2.1).

The main current variability south of Oahu is due to the HLC and the winds variations from north-east to south-west. Vorticity patterns for February 2011 where sporadic south-west winds are present showed that the residual term is

significantly larger than the wind forcing term, probably due to the WRF model not fully representing low frequency south wind patterns (figure 1.9). WRF wind model is a nested model acquiring data from satellite, wind buoys and aircraft (personal communication Dr. Yi-Len Chen) not at the same spatial and temporal resolution as the HFDR, months where winds are variable like February and May it is possible that model can not resolve certain small scale wind patterns that surface currents are detecting. On the contrary August 2011 were trade winds are persistent during the whole month, the spatial similarity between the wind forcing term from the model and the residual from the HFDR is strikingly similar in space and magnitude. The area of positive Wind Stress Curl in both terms is found were the top half of a cyclonic eddie is seen and a strong advection of vorticity is also observed.

Figure 2.2 showed the averaged time series of residual and forcing term, for February, May and August 2011, residual term is similar in space and magnitude as the wind term. However, in October 2011 the wind forcing term is significantly bigger than the residual, since winds are weker and the HLC is stronger (Figure 1.5). The vorticity innput by the HLC can have a significant effect on the increase of the residual term.

Finally, we are not taking into account the error from the second derivation in the nonlinear terms which in February seem larger all over the HFDR coveraged area compared to August where they are only large where wind stress curl is stronger (Figure 2.1). This brings into account that we have ignored a part of the nonlinear

term $\overline{\mathbf{u} \cdot \nabla \zeta} = \overline{\mathbf{u}} \cdot \nabla \overline{\zeta} + \overline{\mathbf{u}' \cdot \nabla \zeta'}$ where over bar denotes a time average and prime represents a deviation from it, even though prime terms appear only at shorter length scales than our measurements and we are assuming it is resolved by the mean flow, more studies in the area are needed to address this issue.

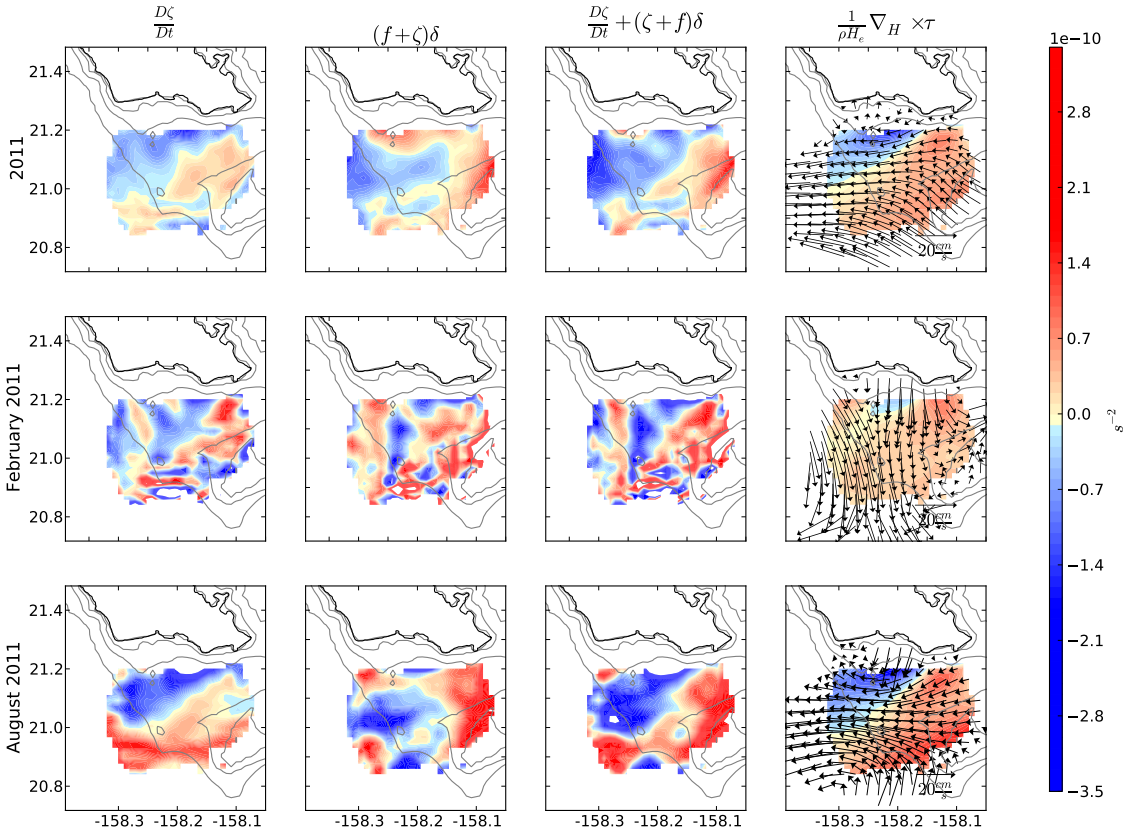

FIGURE 2.1: Averaged vorticity equation terms (eq 2.2) for 2011 (top row), February 2011 (middle row) and August 2011 (bottom row). First column is the advective term, second column is the stretching term and third column is the residual term derived from the sum of the two terms in the vorticity equation which it is assumed to include the external forcing. Fourth column is the wind forcing term with a constant Ekman depth H_E derived from WRF model. Black arrows indicate the averaged low passed surface currents for the time indicated.

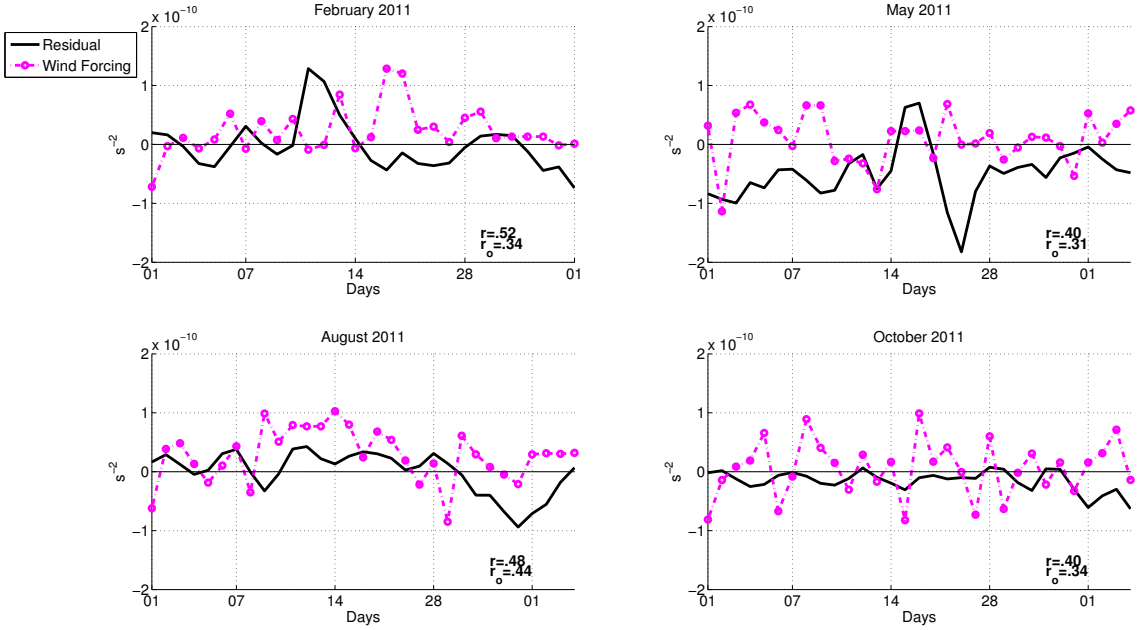

FIGURE 2.2: Time averaged residual term from equation 3 (black line) and wind forcing term derived from WRF model (pink line) for February, May, August and October 2011. 95 % significant correlation of residual term with scaled wind term are denoted as r, 95% significant value is denoted by r_0.

Chapter 3

Numerical Modeling

3.1 Introduction

A numerical model with 4D-Var data assimilation using ROMS (Regional Ocean Modeling System) for the Hawaiian Islands region based on the work of Matthews et al. [2012] and produced by Souza et al. [2014] is analyzed to understand the vertical structure of the currents due to the wind.

The model assimilates satellite Sea Surface Temperature and Sea Surface Height and radial currents from Kalaeloa HFDR at the surface and CTD, ARGO floats and autonomous SeaGliders in the ocean interior. The model is forced with tidal constituents from the TPXO tidal product and atmospheric forcing from

the Weather Research Forecast (WRF) used in Chapter 1 and 2. Lateral boundary conditions were taken from the HYCOM. Model output was produced from January 2011 until August 2012.

Using primitive equations and a hydrostatic balance, the model is a dynamical consistent system where the surface current's noise derived from HFDR is significantly reduced. The assimilation of radials decreased the RMSD values for the model [Souza et al., 2014], see Appendix A for validation of HFDR and ROMS surface currents. Taking advantage of HFDR and model capabilities, this chapter calculates the vorticity balance and empirical orthogonal functions from the model currents to understand the effect of the wind into the water column.

3.2 Methodology

ROMS is a free surface, hydrostatic, primitive equation model discretized with a terrain-following vertical coordinate system [s-level] and vertical resolution increasing toward the surface. Modeled surface currents were output with a 3 hour temporal resolution, 4 km spatial grid and 32 s-levels on the vertical. The model output was 3 day low-passed as the HFDR currents, in order to achieve similar results and valid comparisons. Low passed currents where then interpolated into the HFDR spatial and temporal grid.

The vorticity balance was calculated as in chapter 2 for the surface layer. Mixed layer depth was calculated as the depth where ρ changes 0.125 $kg\ m^{-3}$ in each HFDR grid point. Density was calculated from the salinity and temperature model output using the ITS-90 equation of state at atmospheric pressure.

3.3 Results

ROMS clearly detects the current seasonality due to the wind. Figure 3.1 shows the averaged time series for the whole HFDR domain, on the surface layer there are some eastward and northward reversals observed in March, September 2011 and March-April 2012 where the meridional wind changes direction from north-east to south-west. For the averaged 300-m depth currents, the north and eastward current reversals seen on the surface decreased in magnitude and frequency while in the averaged 1000-m depth the variability completely disappeared and only a north-westward weaker flow was observed.

Empirical Orthogonal Functions derived from the surface assimilated currents accounted for 55%, 13% and 7% of the variance for the first three significant modes respectively. The percentage of variance and spatial EOFs were similar as the EOF's derived from the HFDR surface currents, that is, the first and third spatial function seemed to account for current reversals and the bathymetry effect created for the shallow Penguin Bank. However, the second function was spatially different than the observed from the HFDR domain. Although both HFDR and

model second EOF's spatial functions seemed to account for a cyclonic circulation that is flowing westward close to the coast and eastward away from the coast, the model seems only significant in the deep Kaiwi channel (Figure 3.2). Regardless of those spatial differences, the first and second temporal functions derived by the ROMS model were still significantly correlated to the meridional and wind stress curl term as in the HFDR results.

The 2011 average surface vorticity balance calculated from the ROMS model resulted in similar results as the HFDR balance (Figure 3.3 top row), although stretching, advective and residual terms derived from the ROMS model were an order of magnitude larger than the forcing term derived from the wind, there was a clear spatial similarity. Since the assimilated ROMS currents were atmospherically forced with the same WRF model as with the forcing term, the discrepancies between the terms suggest a bad representation of the ROMS model at the HFDR spatial scales. Furthermore as in the HFDR surface vorticity balance, stretching term is the primary balance of the residual term, with the advective term half an order magnitude smaller than the other terms.

On contrast, for the February averaged vorticity terms (Figure 3.3 second row) where winds present sporadic south-west reversals from the trade-winds, the residual term is stronger on the northwest corner of the area and its magnitude is significantly greater than the wind forcing term derived from the WRF wind model. There is no clear spatial similarity between the ROMS derived residual term and

the forcing term in comparison to the to the HFDR results where their similarity is significantly correlated. For August averaged terms (Figure 3.3 third row), where the trade wind pattern is persistent, there is no spatial similarity between the residual derived from the balance and the wind forcing term derived from the WRF wind model.

Even though the residual term from the vorticity balance for February and August does not seem to represent the wind forcing term, the EOFs did detect the different current behaviors seen on the HFDR since their first and second temporal function were also correlated to the meridional wind and wind stress curl respectively. In addition, to understand how deep the wind affects the currents, vertical EOFs were computed where the wind was best correlated to the HFDR surface currents. Figure 3.4 shows the first three significant vertical modes, the first vertical mode decays linearly from the surface to 300 m, while second and third mode have a maximum at 250 m and 120 m respectively. Mixed layer depth on the whole domain varies between 100 and 200 m which is consistent with the vertical mode 1 decay depth. Since the barotropic mode is associated to the westward HLC, the meridional wind was significantly correlated to the temporal function of the first vertical mode, that is, the eastward reversals observed in both observations and model were detected to be due to the wind variation from north-east to south-west and their effect decayed below the mixed layer depth according to the behavior of the first vertical mode.

3.4 Discussions

The effect of the wind into the surface currents detected by the HFDR was also seen in the ROMS assimilated currents. Eastward and northward current reversals were seen on periods where wind changes frequency and direction. Furthermore, the ROMS EOF's also detected the wind variations and wind stress curl effect on the currents since their temporal functions were correlated with the wind as in Chapter 1. The first Vertical EOF detected the wind variability confined to an upper layer constrained by the Mixed Layer Depth, previous studies have shown a shallow the Mixed Layer Depth of around $\approx 25m$ [Moum et al., 1989; Schneider and Müller, 1990], since vertical mode 1 decays almost linearly from the surface, the Mixed Layer Depth must have a significant effect on the confinement of the wind-driven currents.

The vorticity balance for averaged 2011 ROMS surface currents resulted in an even balance between the advective, stretching and residual term, furthermore, the spatial similarity between the residual and wind forcing term is well correlated and resembles the area of positive wind stress curl due to the wind-wake of the islands east of Oahu (Molokai, Lanai and Maui) to the trade winds [Chavanne et al., 2002]. On the other hand, for the averaged vorticity terms in February and August, the residual and wind forcing term do not resemble each other as with the HFDR results. Since Chapter 2 showed the residual term of the vorticity balance is indeed driven by the wind forcing, the model must be responsible for the

discrepancies in both terms. Souza et al. [2014] compared radials from Kalaeloa HFDR and ROMS and showed that energy on the higher frequencies is lower in the model than in observations. Furthermore, they also found the highest RMSD values between both time series in periods under 1 day and between 16 and 64 days. This explains why the 2011 year average the vorticity balance derived from the ROMS was more accurate than for February and August compared to the HFDR.

The low spatial resolution of ROMS (4 km) compared to the HFDR (2 km) can obscure small scale spatial processes seen on the vorticity balance derived by the HFDR, moreover the variation in Ekman depth can contribute significantly to the differences between residual and wind forcing term, since the positive wind stress curl found in the southeast part of the domain creates a cyclonic circulation, and thus an upward movement of the thermocline, variation in the Ekman depth can be important in the balance resulting in more accurate results for both the HFDR and ROMS vorticity balance. Souza et al. [2014] computed that about 44% of the wind stress curl from the ROMS assimilated model is transferred to the ocean interior by frictional stresses, this is not accounted in the balance shown here, suggesting that unaccounted frictional stresses may play an important role in the accuracy of the residual term derived from the vorticity. More over Calil et al. [2008] showed that although mesoscale cyclones are mostly confined to the lee of the islands, further interaction of these with winds and dissipation processes can possibly transfer momentum and thus vorticity that is also unaccounted.

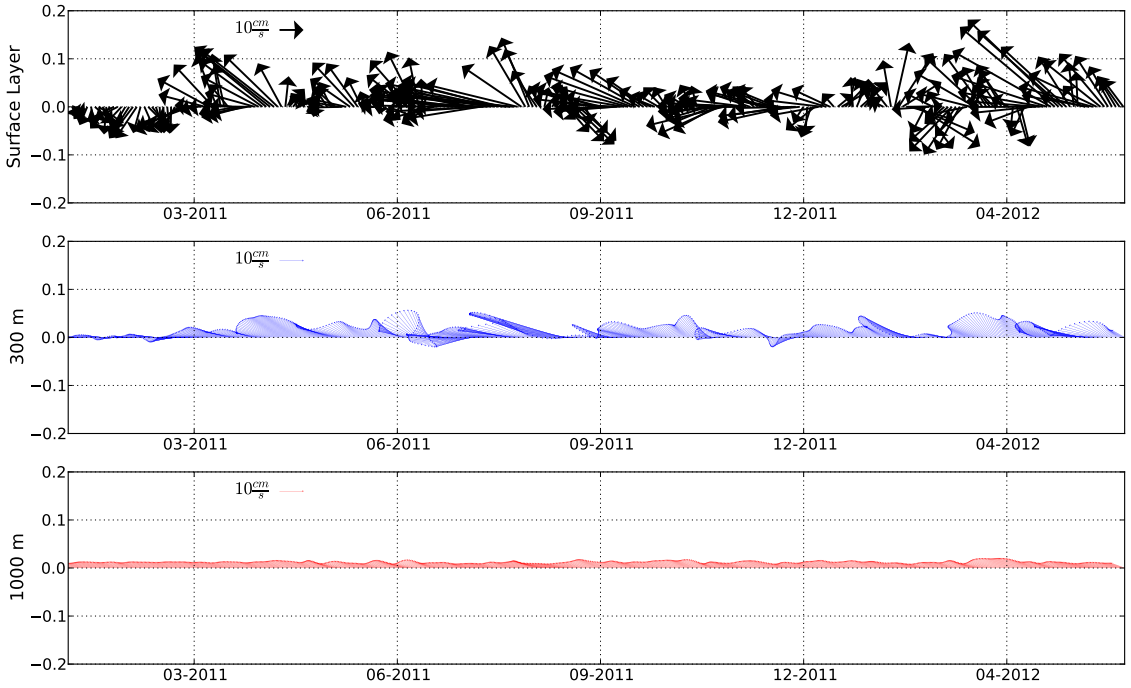

FIGURE 3.1: Spatial average ROMS surface currents for the surface layer (top row), 300 m depth (middle row) and 1000 m depth (bottom row). Top left corner shows the $10ms^{-1}$ scale current, scale is equal in all figures.

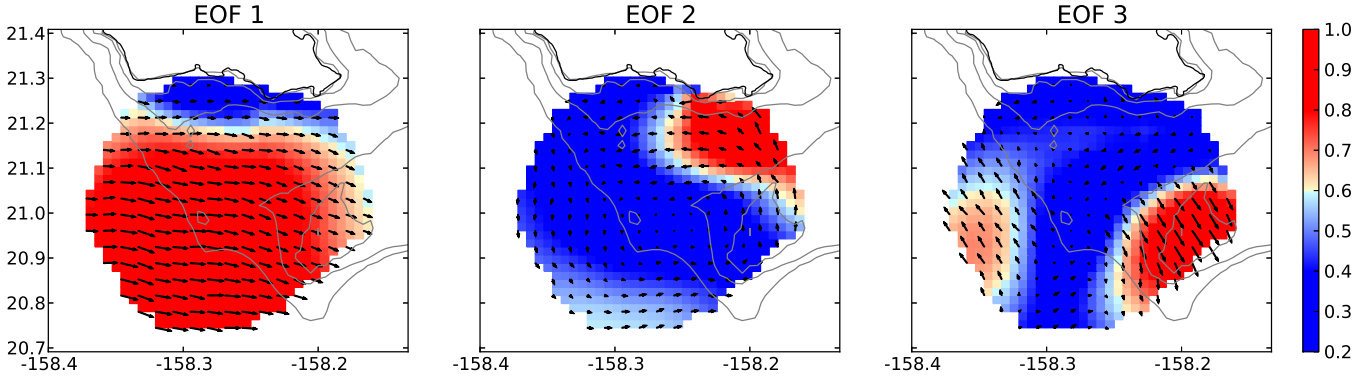

FIGURE 3.2: Significant spatial Empirical Orthogonal Functions (EOF) derived from ROMS assimilated surface currents, EOF 1,2 and 3 accounted for 62%, 12% and 3% of the variance respectively. Averaged reconstructed EOF surface currents are also indicated by black arrows on each figure.

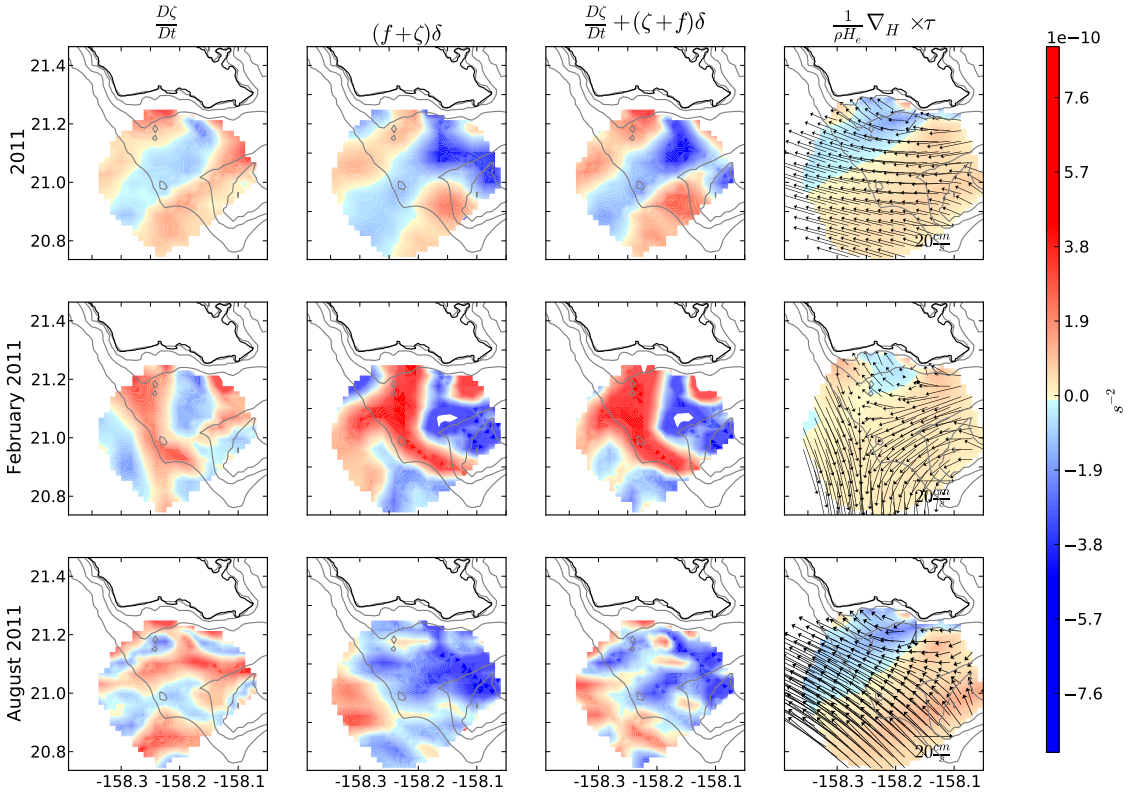

FIGURE 3.3: Averaged vorticity equation terms (eq 2.2) derived by ROMS surface currents for 2011 (top row), February 2011 (middle row) and August 2011 (bottom row). First column is the advective term, second column is the stretching term and third column is the residual term derived from the sum of the three terms in the vorticity equation. Fourth column is scaled to equation 3 wind stress curl derived from model. Black arrows indicate the averaged low passed surface currents for the time indicated.

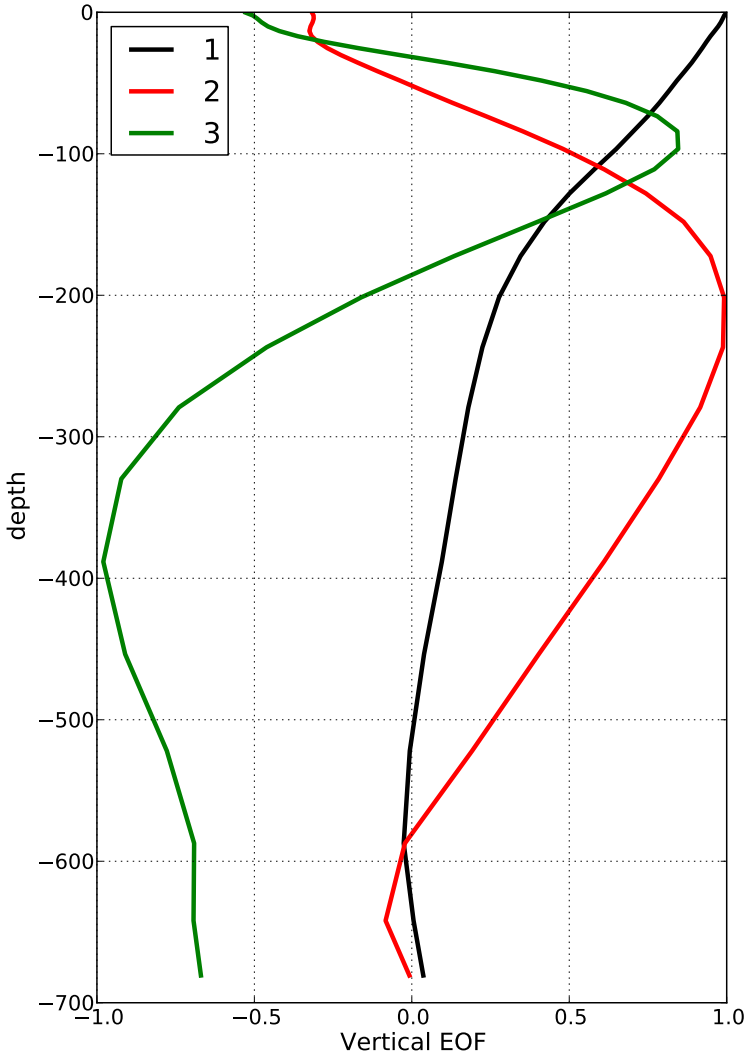

FIGURE 3.4: First three significant vertical EOFs for ROMS currents where wind and HFDR surface currents had the best correlation (See Figure 1.6). Variance accounted for 66%, 15% and 7% of the variance respectively.

Chapter 4

Conclusions

HFDR observations have been used to examine the seasonal patterns south of Oahu. Dynamics seem to be controlled by the westward HLC and the wind patterns observed during different seasons of the year.

While observed westward flows are due to the HLC and HLCC variability, north and east flows appear from the Ekman component of southerly winds which are present in fall and winter. Thus when trade winds are persistent like in summer, the westward flow is enhanced. This is observed from the first EOF accounting for 58% of the variance and which was significant correlated to the meridional wind.

Currents seem equally dominated by the advective and stretching term balanced by an external forcing derived as a residual term from the vorticity equation which is compared to the wind. Balance showed that the residual term from the vorticity balance is indeed due to the wind.

If wind is the main forcing mechanism generating vorticity, two main issues can cause the discrepancy between the residual derived from the vorticity equation and the wind term, while on this study the Ekman layer depth has been constant, variations can significantly alter the wind forcing term and modify the result. Also, model can still not detect small scale wind variations that gave rise to the strong residual term seen in February 2011 and May 2011.

Results in this study showed that small energetic Wind Stress Curl processes can generate vorticity and thus advection of it into other areas. Regions with wind stress curl variations like Hawaii have been observed throughout the world [Chelton et al., 2004]) and their mostly unknown impact can have significant effects on larger scale ocean dynamics.

The inclusion of surface currents derived from the ROMS assimilated currents diminishes the noise due to GDOP near the coast and away from the HFDR sites. Although for calculations such as the vorticity balance which involve second order derivations, the low resolution of the model resulted in a less accurate balance compare to the one derived by the HFDR.

Appendix A

HFDR and ROMS current validations

HFDR validation can be visualized by the correlation between radial currents from a pair of sites [Chavanne et al., 2007]. The correlation approaches -1 along the baseline between the two sites and +1 far offshore where the radials are almost collinear since it should follow the cosine of the angle between the two sites as $r_{12} = \cos(\theta_1 - \theta_2)$ where θ_1 and θ_2 are the angles of radial components from each radar sites to the baseline. Figure A.1a shows the correlation between both HFDR sites, correlations in the majority of the area in figure seem consistent with Figure A.1d.

ROMS surface current can be validated by projecting the vector currents into the radial components of Kalaeloa and KokoHead, Figure A.1 b where radial currents

were assimilated resembles figure A.1d better than Figure A.1c were currents were not assimilated. The difference between both figures shows the impact of assimilating observations into a model, when radial currents are assimilated currents follow almost the exact pattern as the cosine of the angle between the sites, even better than the HFDR observations.

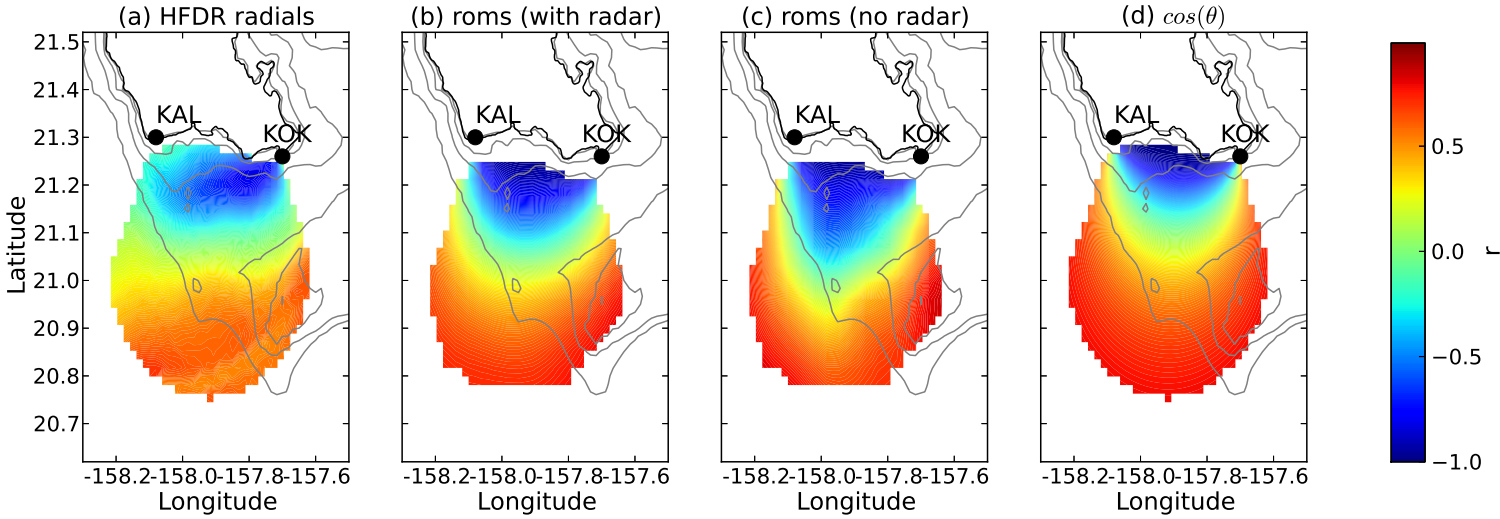

FIGURE A.1: Correlation between KAL and KOK radial currents (a). Correlation between KAL and KOK projected radial currents from ROMS with KAL radial currents assimilated (b). Same as b but no HFDR assimilation (c). Cosine of the angle between both HFDR sites KAL and KOK (d)

f

Appendix B

Geometric Dilution of Precision

Vector currents were estimated on a 2-km Cartesian grid by least square fitting zonal and meridional components to all radial measurements from both of the sites using a 2-km search radius [Lipa and Barrick, 1983; Chavanne et al., 2007]. The normal component is poorly constrained near the baseline between the two sites and azimuthal component far is poorly constrained far from the sites. The currents were assumed to be constant within the search radius, where N is the number of radial measurements available:

$$m_i = n_{ix}u + n_{iy}v + e_i \; i = 1, ...N \tag{B.1}$$

or

$$\mathbf{m} = \mathbf{Nw} + \mathbf{e} \tag{B.2}$$

where $\mathbf{m}$ is the N x 1 vector of radial measurements, $\mathbf{N}$ the N x 2 matrix of the unit radial vectors, $w = [u, v]^T$ the current vector and $\mathbf{e}$ the N x 1 vector of measurements noise and model errors.

An estimate of $\mathbf{w}$ can be obtained by minimizing the sum of squared errors:

$$J = \sum_{i=1}^{N} e_i^2 = \mathbf{e}^T\mathbf{e} \tag{B.3}$$

Solution is :

$$\tilde{\mathbf{w}} = (\mathbf{N}^T\mathbf{N})^{-1}\mathbf{N}^T\mathbf{m} \tag{B.4}$$

The covariance of B4 is:

$$\mathbf{C}_{\tilde{w}\tilde{w}} = (\mathbf{N}^T\mathbf{N})^{-1}\mathbf{N}^T\mathbf{C}_{ee}\mathbf{N}(\mathbf{N}^T\mathbf{N})^{-1} \tag{B.5}$$

where C_{ee} is the covariance of C. If the errors have the same variance and are independent of each other then

$$\mathbf{C}_{ee} = \sigma^2\mathbf{I} \tag{B.6}$$

where $\mathbf{I}$ is the unit matrix. Then the covariance of $\tilde{\mathbf{w}}$ becomes:

$$\mathbf{C}_{\tilde{w}\tilde{w}} = \sigma^2(\mathbf{N}^T\mathbf{N})^{-1} \tag{B.7}$$

This expression of $\sigma = 1$ becomes the GDOP. Figure B.1a shows the principal axes of $\mathbf{C}_{\tilde{w}\tilde{w}}$. In the present study data with GDOP greater than 4 was discarded. This high value was required since the HFDR configuration increased the GDOP substantially.

Figure B.1 b and c show the variance ellipses derived from HFDR and surface ROMS currents respectively. In most of the area the axis of maximum variance is parallel to the coast, except close to the coast and away from the HFDR sites where GDOP poorly constrains the meridional and zonal component for the u and v vector currents and creates unrealistic values. However in the rest of the area, the spatial similarity between ellipses from ROMS and HFDR currents is remarkable, with ellipses increasing away from the coast and tilting towards the northwest following the bathymetry contours.

Color shows the Eddy Kinetic Energy (EKE) from each of the ellipses, energy increases away from the coast in both figures whereas the GDOP creating from the HFDR creates regions of high EKE close to the coast and away from the sites.

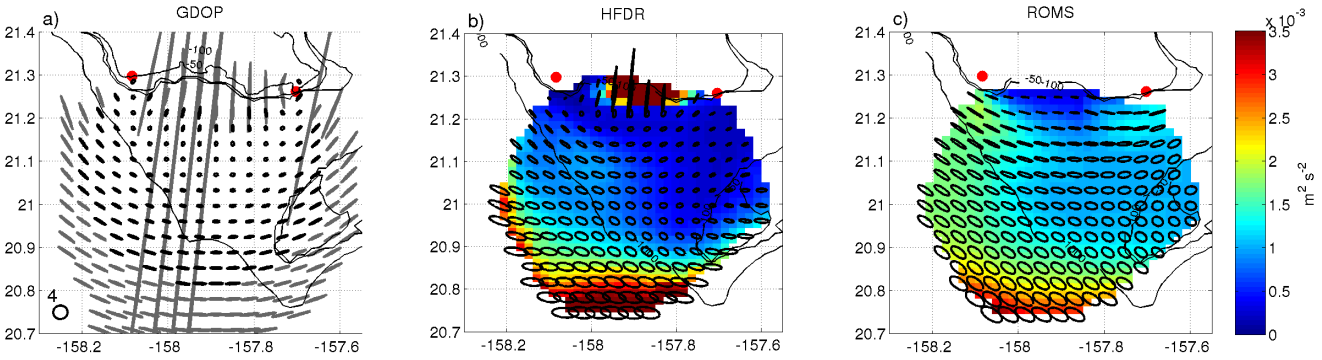

FIGURE B.1: a)Geometric Dilution of Precision (GDOP) ellipses from the pair of HFDR sites KOK and KAL (red dots), values greater than 4 were discarded from the dataset and are shown in light grey. Remaining values are shown in black. b) Variance ellipses for the 3 day low-passed HFDR, colorbar indicates the EKE in $m^2 s^{-2}$. c) Same as b but for the surface layer of the ROMS assimilated currents

Bibliography

Barton, Eric D; Basterretxea, Gotzon; Flament, Pierre; Mitchelson-Jacob, E Gay; Jones, Bethan; Arístegui, Javier, and Herrera, Felix. Lee region of gran canaria. *Journal of Geophysical Research: Oceans (1978–2012)*, 105(C7):17173–17193, 2000.

Calil, Paulo HR; Richards, Kelvin J; Jia, Yanli, and Bidigare, Robert R. Eddy activity in the lee of the hawaiian islands. *Deep Sea Research Part II: Topical Studies in Oceanography*, 55(10):1179–1194, 2008.

Cass, J. Eddies an currents of the hawaiian islands. *Master thesis. Sch. of Ocean and Earth Sci. and Technol. Univ. of Hawaii at Manoa*, page 114, 2010.

Chapman, RD; Shay, LK; Graber, HC; Edson, JB; Karachintsev, A; Trump, CL, and Ross, DB. On the accuracy of hf radar surface current measurements: Intercomparisons with ship-based sensors. *Journal of Geophysical Research: Oceans (1978–2012)*, 102(C8):18737–18748, 1997.

Chavanne, C; Janeković, Ivica; Flament, P; Poulain, P-M; Kuzmić, Milivoj, and Gurgel, K-W. Tidal currents in the northwestern adriatic: High-frequency radio

observations and numerical model predictions. *Journal of Geophysical Research: Oceans (1978–2012)*, 112(C3), 2007.

Chavanne, C; Flament, P; Carter, G; Merrifield, M; Luther, D; Zaron, E, and Gurgel, KW. The surface expression of semidiurnal internal tides near a strong source at hawaii. part i: Observations and numerical predictions*. *Journal of Physical Oceanography*, 40(6):1155–1179, 2010.

Chavanne, Cédric; Flament, Pierre; Lumpkin, Rick; Dousset, Bénédicte, and Bentamy, Abderrahim. Scatterometer observations of wind variations induced by oceanic islands: Implications for wind-driven ocean circulation. *Canadian Journal of Remote Sensing*, 28(3):466–474, 2002.

Chelton, Dudley B; Schlax, Michael G; Freilich, Michael H, and Milliff, Ralph F. Satellite measurements reveal persistent small-scale features in ocean winds. *Science*, 303(5660):978–983, 2004.

Firing, Eric; Qiu, Bo, and Miao, Weifeng. Time-dependent island rule and its application to the time-varying north hawaiian ridge current*. *Journal of physical oceanography*, 29(10):2671–2688, 1999.

Gurgel, K-W; Antonischki, G; Essen, H-H, and Schlick, T. Wellen radar (wera): a new ground-wave hf radar for ocean remote sensing. *Coastal Engineering*, 37 (3):219–234, 1999.

Jia, Y; Calil, PHR; Chassignet, EP; Metzger, EJ; Potemra, JT; Richards, KJ, and Wallcraft, Alan J. Generation of mesoscale eddies in the lee of the hawaiian islands. *Journal of Geophysical Research: Oceans (1978–2012)*, 116(C11), 2011.

Kobashi, Fumiaki and Kawamura, Hiroshi. Seasonal variation and instability nature of the north pacific subtropical countercurrent and the hawaiian lee countercurrent. *Journal of Geophysical Research: Oceans (1978–2012)*, 107(C11): 6–1, 2002.

Kundu, Pijush K. Ekman veering observed near the ocean bottom. *Journal of Physical Oceanography*, 6(2):238–242, 1976.

Large, WG and Pond, S. Open ocean momentum flux measurements in moderate to strong winds. *Journal of physical oceanography*, 11(3):324–336, 1981.

Lipa, B and Barrick, D. Least-squares methods for the extraction of surface currents from codar crossed-loop data: Application at arsloe. *Oceanic Engineering, IEEE Journal of*, 8(4):226–253, 1983.

Lumpkin, CF. Eddies an currents of the hawaiian islands. *Ph.D. thesis. Sch. of Ocean and Earth Sci. and Technol. Univ. of Hawaii at Manoa*, page 282, 1998.

Lumpkin, Rick and Flament, Pierre. Lagrangian statistics in the central north pacific. *Journal of marine systems*, 29(1):141–155, 2001.

Lumpkin, Rick and Flament, Pierre J. Extent and energetics of the hawaiian lee countercurrent. *Oceanography*, 26(1):58–65, 2013.

Matthews, Dax; Powell, BS, and Janeković, Ivica. Analysis of four-dimensional variational state estimation of the hawaiian waters. *Journal of Geophysical Research: Oceans (1978–2012)*, 117(C3), 2012.

Moum, James N; Caldwell, Douglas R, and Paulson, Clayton A. Mixing in the equatorial surface layer and thermocline. *Journal of Geophysical Research: Oceans (1978–2012)*, 94(C2):2005–2022, 1989.

Patzert, WC. Eddies in hawaiian waters. *HIG*, 69(8):55, 1969.

Pawlowicz, Rich; Beardsley, Bob, and Lentz, Steve. Classical tidal harmonic analysis including error estimates in matlab using t_tide. *Computers & Geosciences*, 28(8):929–937, 2002.

Pullen, Julie; Doyle, James D; May, Paul; Chavanne, Cedric; Flament, Pierre, and Arnone, Robert A. Monsoon surges trigger oceanic eddy formation and propagation in the lee of the philippine islands. *Geophysical Research Letters*, 35(7), 2008.

Qiu, Bo and Durland, Theodore S. Interaction between an island and the ventilated thermocline: Implications for the hawaiian lee countercurrent. *Journal of physical oceanography*, 32(12):3408–3426, 2002.

Qiu, Bo; Koh, Deborah A; Lumpkin, Claude, and Flament, Pierre. Existence and formation mechanism of the north hawaiian ridge current. *Journal of Physical Oceanography*, 27(3):431–444, 1997.

Schneider, Niklas and Müller, Peter. The meridional and seasonal structures of the mixed-layer depth and its diurnal amplitude observed during the hawaii-to-tahiti shuttle experiment. *Journal of physical oceanography*, 20(9):1395–1404, 1990.

Schudlich, Rebecca R and Price, James F. Observations of seasonal variation in the ekman layer. *Journal of physical oceanography*, 28(6):1187–1204, 1998.

Souza, João; Powell, BS; Castillo-Trujillo, Alma, and Pierre, Flament. The vorticity balance of the ocean surface in hawaii from a regional reanalysis, 2014. Submitted to Journal of Physical Oceanography.

Yu, Zuojun; Maximenko, Nikolai; Xie, Shang-Ping, and Nonaka, Masami. On the termination of the hawaiian lee countercurrent. *Geophysical research letters*, 30 (5):1215, 2003.